Biosensors and Bioelectronics 123 (2019) 59–68

Contents lists available at ScienceDirect

Biosensors and Bioelectronics

journal homepage: www.elsevier.com/locate/bios

Novel nanoarchitecture of Co-MOF-on-TPN-COF hybrid: Ultralowly sensitive bioplatform of electrochemical aptasensor toward ampicillin

Xiaokang Liu[a], Mengyao Hu[b], Minghua Wang[b], Yingpan Song[b], Nan Zhou[a,*], Linghao He[b], Zhihong Zhang[b,*]

[a] Department of Orthopedics, The First Affiliated Hospital of Zhengzhou University, Zhengzhou 450000, PR China
[b] Henan Provincial Key Laboratory of Surface and Interface Science, Zhengzhou University of Light Industry, No. 136, Science Avenue, Zhengzhou 450001, PR China

ARTICLE INFO

Keywords:
Covalent organic frameworks
Cobalt-based metal–organic frameworks
Co-MOF@COF
Electrochemical aptasensor
Detection of ampicillin

ABSTRACT

Owning to the misuse of the antibiotics in animal husbandry and agriculture, it is highly urgent to determine the quantification of antibiotics in biological systems by the simple, sensitive, and fast method. In this work, a novel nanoarchitecture of Co-based metal-organic frameworks (Co-MOF) and terephthalonitrile-based covalent organic framework (TPN-COF) was synthesized (represented by Co-MOF@TPN-COF), followed by the exploitation as the bioplatform of non-label aptasensor for detecting the most frequently used β-lactam antibiotics, ampicillin (AMP). The new porous hybrid material of Co-MOF@TPN-COF was synthesized by adding the as-prepared TPN-COF into the Co-MOF preparation system. The multilayered Co-MOF@TPN-COF nanosheets exhibit a high specific surface area (52.64 m^2 g^{-1}), nitrogen-rich groups and excellent electrochemical activity. As a result, large amounts of aptamer strands can be bound over the Co-MOF@TPN-COF nanosheets owning to the strong π–π stacking and hydrogen bonds. When detecting AMP by the electrochemical impedance spectroscopy, the fabricated Co-MOF@TPN-COF-based aptasensor exhibits an ultra-low detection limit of 0.217 fg mL^{-1} within the AMP concentration from 1.0 fg mL^{-1} to 2.0 ng mL^{-1}, which was superior to those previously reported in literatures. In addition, this proposed aptasensor also shows high selectivity, good reproducibility and stability, acceptable regenerability, and favorable applicability in human serum, river water and milk. Therefore, the proposed Co-MOF@TPN-COF-based aptasensor has a great promise to be applied as a powerful tool in the fields of food safety.

1. Introduction

As one of the most frequently used β-lactam antibiotics, ampicillin (AMP) has been used extensively in medicine and agriculture to treat bacterial infections (Drawz and Bonomo, 2010). In the past decades, many efforts have been made to develop efficient methods to detect the AMP residues in agricultural products and waters since the misuse of AMP can lead to allergic reactions, breathing difficulties, and seizures in humans (Moura et al., 2012), including microbiological assays (Chakraborty et al., 2018), enzyme-linked immunosorbent assays (Wang et al., 2015), Raman spectroscopy (Clarke et al., 2005), fluorescence detection (Das et al., 2017), and so on. These methods suffer from the drawbacks of long analysis time, high cost, the need for skilled manpower, sophisticated instruments or unsatisfactory sensitivity. It would limit them to behave as the on-site assays in practical applications. Consequently, there is an urgent need for rapid, accurate, sensitive, and economical methods for detecting antibiotic residues in food.

Aptamers are single-stranded and synthetic oligonucleotides (DNA or RNA) fold into 3-dimensional shapes, which are capable of binding with high affinity to a target molecule by non-covalently (Tombelli et al., 2005). Utilizing the systematic evolution of ligands by exponential enrichment (SELEX) method from a sequence library, aptamers could be selected in vitro (Klug and Famulok, 1994). Owning to their unique properties, aptamers have been used in a wide range of applications, such as medicine, cell and microbiology, and analytical chemistry. In particular, aptamer-based biosensors and assays are being investigated as possible alternatives to conventional antibody-based technology. As compared with monoclonal antibodies, aptamers exhibit distinct advantages involving easier synthesis, less expensive, better stability toward a broad range of binding targets, lower molecular weight, and more sustainable to repetitious denaturation and renaturation (Bunka and Stockley, 2006; Meng et al., 2016). Considering the advantages of the aptamer sensors and the electrochemical techniques, the electrochemical aptasensors have attracted considerable

* Corresponding authors.
E-mail addresses: fcczhoun@zzu.edu.cn (N. Zhou), 2006025@zzuli.edu.cn (Z. Zhang).

https://doi.org/10.1016/j.bios.2018.09.089
Received 3 August 2018; Received in revised form 18 September 2018; Accepted 27 September 2018
Available online 27 September 2018
0956-5663/

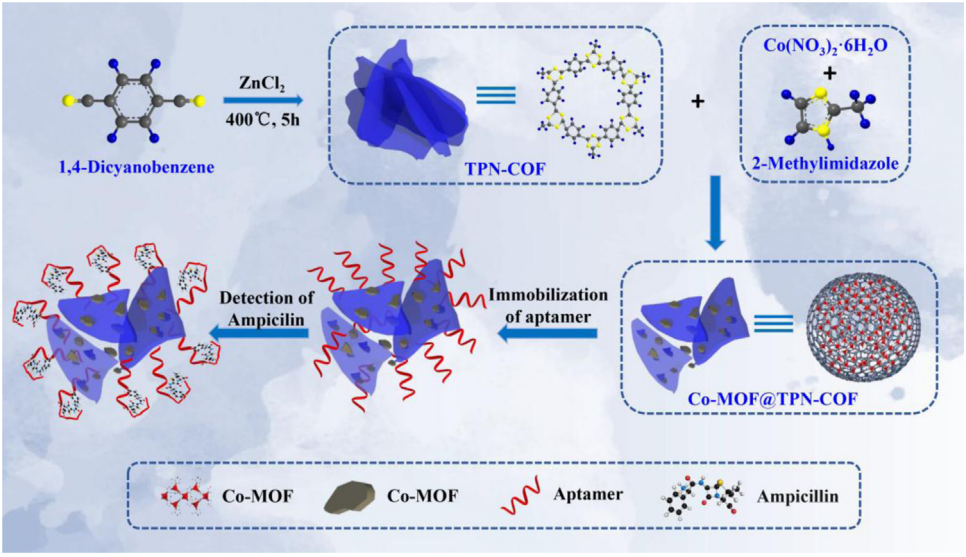

Scheme 1. The schematic diagram of the construction of the Co-MOF@TPN-COF-based aptasensor for detecting Ampicillin.

attentions for the assessment of food quality and safety owing to high sensitivity, simplicity and rapid response (Lan et al., 2017; Vasilescu and Marty, 2016; Zhang et al., 2018). Especially, various electrochemical aptasensors were constructed to detect various hazard molecules. For instance, DNA functionalized gold nanoparticles (Wang et al., 2018) and a self-assembled monolayer (Yang et al., 2017) were employed as the scaffold as AMP aptasensor, only giving the detection limit of pM or nM level. A target-initiated T7 exonuclease assisted signal amplification method was proposed to detect AMP, supplying a LOD of 4.0 pM (Wang et al., 2016a, 2016b), but showing a complex procedure. Since the performances of the electrochemical biosensors depend intimately on the properties of the adopted materials, a variety of nanomaterials with unique electronic and catalytic properties as well as high specific surface areas are increasingly employed as effective signal enhancers, such as carbon nanotubes, graphene, quantum dots, metal or metal oxide nanoparticles, etc (Palchetti and Mascini, 2012; Wang et al., 2016a, 2016b; Zhu et al., 2015).

Recently, porous crystalline materials, composed of both inorganic and organic materials, such as zeolites, metal-organic frameworks (MOFs), covalent organic frameworks (COFs), and porous organic cages, have been widely developed because of their well-defined topological structures and inherent porosities (Chen et al., 2018a, 2018b; Lin et al., 2017). Thanks to their attracting features, MOFs and COFs have been extensively investigated for various applications including gas storage and separation, drug delivery, catalysis, heterogeneous catalysis, semiconductor and photoconductor, sensing, and so on (Feng et al., 2012; Kreno et al., 2012; Lee et al., 2009; Zhao et al., 2018). Specifically, the unique planar structure, sizable specific surface area, the π–π stacking interaction, and hydrogen bonding of MOFs and COFs would enlarge the loading efficiency and surface concentration of probe biomolecules (Guo et al., 2017; Li et al., 2017; Ning et al., 2018; Peng et al., 2017a, 2017b). So far, various MOFs and COFs materials, including zirconium-based MOF (Su et al., 2017; Zhang et al., 2017a, 2017b), Cu(HBTC)-1/Fe_3O_4-AuNPs (Tan et al., 2017), and ultrathin COF nanosheets (Zhao et al., 2015), were exploited as the sensitive layers for biosensors or immunsensors. Among many MOFs, zeolitic imidazolate frameworks (ZIFs) are an extensive class of hybrid solid-state materials self-assembled from metal ions or clusters with judiciously designed molecular building blocks into desired frameworks via coordination bonds with 2-methylimidazole (Shi et al., 2010). Thereby, ZIF contains stacking π-electron systems of the bridging five-membered imidazolate ring, which can strongly adsorb single-stranded DNA (ssDNA) through π–π stacking to develop various biosensors (de Silva et al., 1997; Feng et al., 2018). Nevertheless, the strategy for enhancing the sensing performance of MOFs as electrochemical sensors is always an issue of concern, and the key point is to improve the conductivity of MOFs (Wen et al., 2018). MOF-based hybrid materials have been prepared by hybridizing MOFs with other functional materials, such as metal nanoparticles (NPs), polymers, and other MOFs, which could inherit the structural traits of individual components and exhibit new properties (Chen et al., 2018a, 2018b; Xie et al., 2015). At moment, few works were reported about the combination of MOFs and COFs and their applications (Fu et al., 2016; Peng et al., 2017a, 2017b; Zhuang et al., 2017). Howbeit, the applications of MOFs@COFs composite mainly focus on the photocatalysis, electrocatalyst, or gas separation membrane, not in the fields of biosensings and biomedicals. Combining the sensitivity and specificity of the aptasensors, feasible operations of electrochemical techniques, and excellent electrochemical activity and strong bio-affinity toward biomolecules of porous organic frameworks, it would be very significant to explore a novel MOF@COF composite-based biosensor to sensitively detect race AMP in aqueous solutions. A kind of nitrogen-rich COFs, amorphous terephthalonitrile-derived nitrogen-rich networks (denoted as TPNs), has been synthesized through trimerization reactions of terephthalonitrile monomers (Kuhn et al., 2008a, 2008b), and successfully engaged in different fields (Chan-Thaw et al., 2010). Therefore, one can anticipate that TPN can facilitate the aptamer strands to anchor owning to its intrinsic features including high surface area, well-defined pore structure, and heteroatom-doped organic skeleton.

Inspired by these reported studies on MOFs as the sensitive platforms for aptasensors and our previous research studies on the fabrication of MOFs-based aptasensors (Guo et al., 2017; Su et al., 2017), we synthesized a novel MOF-on-COF composite and further explored its application in constructing a sensitive electrochemical aptasensor for AMP detection (Scheme 1) for the first time. In the present work, Co-MOF was in situ grew on the TPN surface (represented by Co-MOF@TPN-COF), thus forming a novel kind of MOF@COF composite. The synthesized Co-MOF@TNN-COF simultaneously exhibits the features of MOFs and COFs, including (i) rich nitrogen-related functional groups; (ii) excellently electrochemical activity due to the strong synergistic effect between the rich triazine rings in TPN-COF and framework containing in Co-MOF; and (iii) highly strong bioaffinity interaction between the aptamer strands and the Co-MOF@TPN-COF matrix because of π–π stacking and hydrogen bonding. As such, the fabricated Co-MOF@TPN-COF-based aptasensor exhibits extremely low detection limit (0.217 fg mL^{-1}) within the AMP concentration from 1.0 fg mL^{-1}

to 2.0 ng mL^{-1}. Concurrently, it also shows high selectivity, good reproducibility and stability, and acceptable applicability.

2. Experimental section

2.1. Materials and chemicals

$ZnCl_2$ was purchased from Sailboat Chemical Reagent Technology Co., Ltd. (Tianjin, China). 2-methylimidazole was obtained from Kemi European Chemical Reagent Co., Ltd. (Tianjin, China). $Co(NO_3)_2{\cdot}6H_2O$ and terephthalonitrile were purchased from Aladdin Reagent Co. Ltd. AMP, doxorubicin hydrochloride (ADR), tobramycin (TOB), streptomycin (RFP), kanamycin (Kana), penicillin, cafazolin, prostate specific antigen (PSA), and bovine serum albumin (BSA) were purchased from Solarbio Life Sciences Reagent Co. Ltd. (Beijing, China). $CaCl_2$ and NaCl were obtained from Yili Fine Chemicals Co., Ltd. (Beijing, China). All of the other chemicals used were of analytical reagent grade and used without further purification. Milli-Q water ($\geq$ 18.2 Ω cm) was used throughout the experiments. The AMP targeted aptamer sequence is listed as follows: 5′-TTAGTTGGGGTTCAGTTGG-3′ (Yu and Lai, 2018).

2.2. Synthesis of the Co-MOF@TPN-COF hybrid

2.2.1. Synthesis of TPN-COF

According to the reported literature (Kuhn et al., 2008a, 2008b), TPN-COF was synthesized using terephthalonitrile as monomer, whereas $ZnCl_2$ was used as catalyst. These two components were placed in a mortar and fully grind. Afterward, the mixture was calcinated in a tube furnace under a N_2 flow at 400 °C for 5 h with the rate of 5 °C min^{-1}. After cooling to room temperature, the resultant powder was washed with Milli-Q water several times and finally dried under vacuum at 60 °C for 10 h.

2.2.2. Synthesis of Co-MOF and Co-MOF@TPN-COF hybrid

Co-MOF was synthesized according to the method proposed by He et al. (Xia et al., 2018) with a few modifications. Briefly, 0.582 g of $Co(NO_3)_2{\cdot}6H_2O$ and 1.3 g of 2-methylimidazole were dispersed in 20 mL of Milli-Q water, separately. Afterward, two resultant solutions were mixed together and keep standing at room temperature for 4 h. The obtained product was washed with Milli-Q water several times, following by drying in vacuum drying oven at 60 °C for 10 h. As for the preparation of the Co-MOF@TPN-COF nanoarchitecture, 8.0 mg of TPN-COF powder was added into the above synthesis system of Co-MOF. Finally, the Co-MOF, TPN-COF, and Co-MOF@TPN-COF hybrid were obtained and stored for further use.

2.3. Preparation of phosphate buffered saline, aptamer, AMP, and real sample solutions

Phosphate buffered solution (PBS, 0.01 M, pH 7.4) was prepared by mixing 0.242 g KH_2PO_4, 1.445 g $Na_2HPO_4{\cdot}12H_2O$, 0.200 g KCl, and 8.003 g NaCl in 1.0 L of Milli-Q water. The stock solution of aptamer (100 nM), AMP and other analogues (10 pg mL^{-1}) were prepared using PBS and stored at 4 °C. The electrolyte solution was prepared just before use by dissolving 1.650 g of $K_3Fe(CN)_6$ and 2.111 g of $K_4Fe(CN)_6$ in 1.0 L of PBS.

The human serum was obtained from The First Affiliated Hospital of Zhengzhou University; river water was got from the Xushui River near our school, and milk was bought from the supermarket. The human serum and river water were diluted 500 times with 0.01 M PBS (pH 7.4), and then filtered with 0.45 μm filtration membrane. The milk was mixed with 0.2 mL NaOH (1 mM) and 10 mL of acetonitrile with 20% concentration of NH_4OH. The mixture was then swirled to get the supernatant. The as-treated milk solution was diluted 500 times with 0.01 M PBS (pH 7.4), and then filtered with 0.45 μm filtration membrane. Different concentrations of AMP (0.001, 0.01, 0.1, 1, 10, 100, 1000 pg mL^{-1}) were spiked into the three treated human serum, river water and milk solutions for real sample analysis.

2.4. Pretreatment of bare Au electrode

Bare Au electrodes (AE) with 0.3 mm diameter was cleaned prior to use. The AE was polished with 0.05 μm alumina slurry and then sonicated in piranha solution (*v/v*, 3:1 H_2SO_4/H_2O_2), ethanol and water for 15 min, respectively. Afterwards, the AE was electrochemically washed through oxidation and reduction cycling in 0.5 M H_2SO_4 from − 0.2 to 1.6 V, and then rinsed with Milli-Q water and dried under a N_2 stream.

2.5. Fabrication of Co-MOF-, TPN-COF-, Co-MOF@TPN-COF-based aptasensors for detecting AMP

Firstly, the dispersions of three samples, including Co-MOF, TPN-COF, Co-MOF@TPN-COF, were prepared by the following steps. Co-MOF, TPN-COF, or Co-MOF@TPN-COF powder (1.0 mg) was added to Milli-Q water (1.0 mL) and thoroughly mixed using ultrasonic until a homogeneous suspension was obtained.

Subsequently, 5.0 μL of Co-MOF@TPN-COF suspension (1.0 mg mL^{-1}) was dropped onto the surface of pre-treated bare Au electrode (AE) and then dried at room temperature for 5 h (denoted as Co-MOF@TPN-COF/AE). Afterward, the modified AE was immersed in the aptamer solution (100 nM) for 30 min at 4 °C (denoted as Apt/Co-MOF@TPN-COF/AE) to ensure that the aptamer strands anchor onto the modified AE surface until saturated. Finally, the Apt/Co-MOF@TPN-COF/AE was immersed in AMP solutions with different concentrations for further electrochemical measurements (denoted as AMP/Apt/Co-MOF@TPN-COF/AE). As for comparison, Co-MOF and TPN-COF-based aptasensors were also fabricated using the similar method.

2.6. Characterizations

The powder X-ray diffraction (PXRD) measurements were performed on a Rigaku D/Max-2500 X-ray diffractometer using Cu K_α radiation. The chemical structure and component of all samples were analyzed by Fourier transform infrared spectroscopy (FT-IR) (Bruker TENSOR27, Germany) and X-ray photoelectron spectroscopy (XPS) (ESCALAB 250Xi photoelectron spectrometer, Scientific Thermo Fisher, USA), respectively. Field emission scanning electron microscopy (FE-SEM) was conducted using a JSM-6490LV scanning electron microscope. High-resolution transmission electron microscopy (HR-TEM) measurements were performed using a JEOL JEM-2100 system with a field emission gun of 200 kV. The specific surface areas of all samples were carried out by the method of Brunauer-Emmett-Teller (BET) using a Micromeritics ASAP2022 instrument at the temperature of liquid nitrogen. Prior to each measurement, the samples were degassed at 573 K for 8 h.

2.7. Electrochemical measurements

All electrochemical measurements, including cyclic voltammetry (CV) and electrochemical impedance spectroscopy (EIS) were conducted on a CHI 660E electrochemical workstation (Shanghai Chenhua, China) with a traditional three-electrode system. The bare AE or modified AE, Ag/AgCl (saturated KCl) and Pt wire were used as working electrode, reference electrode and counter electrode, respectively. CV curves were measured in the mixture of 5.0 mM $K_3[Fe(CN)_6]/K_4[Fe(CN)_6]$ (1:1) as a redox probe dissolved in 0.10 M PBS at potentials ranging from − 0.2 to 0.8 V vs. Ag/AgCl (saturated KCl) at the scan rate of 100 mV s^{-1}. EIS spectra were recorded at a bias potential of 0.21 V vs. Ag/AgCl (saturated KCl) and 5 mV amplitude in the frequency ranging from 0.01 Hz to 100 kHz. The EIS data were analyzed using Zview2 software (Fig. S1), of which EIS spectra were simulated

using an equivalent circuit consisted of solution resistance (R_s), charge-transfer resistance (R_{ct}), constant-phase element (CPE), and Warburg impedance (W_o) (the inset in Fig. S1). Each measurement was repeated at least three times.

3. Results and discussion

3.1. Design mechanism of the Co-MOF@TPN-COF-based aptasensor

In the present work, the bilayer nanostructured Co-MOF@TPN-COF composite was synthesized by the hybridization of Co-MOF and the TPN-COF (Scheme 1**)**. As such, the integration of TPN-COF and Co-MOF enables the composite with several advantages, including high surface specific area, excellent electrochemical activity, and strong bioaffinity toward aptamer (Jiang et al., 2018; Li et al., 2017). Consequently, large amounts of aptamer strands can anchor over the Co-MOF@TPN-COF composite through the π–π stacking effect (Li et al., 2017). Additionally, owning to the porous nanostructure, it can lead to the aptamer penetration into the composite interior and adsorption onto the surface owning to its mesoporous structure (Zhang et al., 2017a, 2017b). In the presence of the target molecules, AMP, the anchored aptamer strands will be presumed to change its conformation and flexibility to bind with AMP (Yu et al., 2018). Each step of the atpasensor fabrication can alter the electron transfer between the electrode and electrolyte solution, which can be determined by the electrochemical techniques.

3.2. Surface morphologies of all samples

FE-SEM and HR-TEM characterizations were employed to evaluate the surface morphologies of three samples, including Co-MOF, TPN-COF, and Co-MOF@TPN-COF. Fig. S2a shows that the SEM image of the as-prepared Co-MOF displays typical leaf-like ZIF lamellae structure, which possesses a shape with smooth surface and uniform average size of about 12 μm and width of 5 μm (Fig. S2b). The SEM images of TPN-COF show two dimensional nanosheets with irregular shape, which are also aggregated into multilayered nanostructure (Figs. S2c and S2d). The detailed microstructure of the three samples is further investigated by HR-TEM. The TEM images of Co-MOF (Figs. S3a and S3b) clearly demonstrate that it is composed of thin irregular nanosheets, for which the transparent layers change from bright to dark with increasing the layer thickness. As seen from the HR-TEM image of Co-MOF (Fig. S3c), it illustrates that the lattice space is 0.233 nm in the crystalline domain, which is consistent with (311) lattice plane of Co_3O_4 (Xiong et al., 2011). TEM images of TPN-COF display highly ultrathin nanosheets with wrinkled surface. A closer observation by HR-TEM in Fig. S3f shows two lattice spaces of 0.247 and 0.281 nm corresponding to the (101) and (100) lattice planes of ZnO, respectively, which further proves the existence of Zn element. Similarly, the Co-MOF@TPN-COF has a multilayer nanostructure with wrinkled surface (Fig. 1**a-d**). From the HR-TEM image (Fig. 1**e**), the coexistence of the lattice space of 0.233 nm and 0.247 nm are observed, suggesting the successful combination of Co-MOF and TPN-COF.

3.3. Chemical structure and components of all samples

The chemical and crystal structure of all samples were characterized by FT-IR and XRD, respectively. As displayed in Fig. 2**a**, the characteristic adsorption bands at 1560 and 1300 cm^{-1} indicates the formation of the triazine rings in FT-IR spectrum of TPN-COF (Bojdys et al., 2010). The absence of the carbonitrile band at 2230 cm^{-1} suggests that the occurrence of the trimerization reaction of terephthalonitrile (Kuhn et al., 2008a, 2008b). As for the Co-MOF, the subtantial adsorption band at 595 cm^{-1} was observed, corresponding to Co−O (Qi et al., 2013), whereas the peaks around 1142 and 1302 cm^{-1} belong to the C–H vibrations, along with the peak at 1560 cm^{-1} corresponded to C=N vibration (Yang et al., 2018). After the combination of TPN-COF and Co-MOF, i.e., Co-MOF@TPN-COF, the similar characteristic spectrum is observed with that of the TPN-COF, suggesting their similar chemical structure. The PXRD patterns of all samples are illustrated in Fig. 2**b**. The weak intensity of TPN-COF indicates its low crystallinity. The PXRD of Co-MOF exhibits the similar diffraction peaks with those reported in the literature, suggesting the successful preparation of Co-MOF (Gross et al., 2012). As for the Co-MOF@TPN-COF, the weak intensity of its PXRD also indicates the low crystallinity, further proving the successful combination of Co-MOF and TPN-COF.

Additionally, the N_2 adsorption-desorption isotherms of three samples were obtained (Fig. 2**c**), from which the specific surface areas were calculated. It displays that the specific surface areas of Co-MOF, TPN-COF, and Co-MOF@TPN-COF hybrid are evaluated to be 46.72, 1.81, and 52.64 $m^2\ g^{-1}$, respectively. All of these results indicate that the nanostructured Co-MOF@TPN-COF nanosheets are feasible to disperse in the aqueous solution and easy to employ as the scaffold for the immobilization of probe molecules owing to its high specific surface area.

The XPS survey scan spectra of three samples are displayed in Fig. 2**d**, in which the C 1*s* (284.6 eV), N 1*s* (400.1 eV), and O 1*s* (530.2 eV) are coexisted in three samples. Beyond these, the strong signal of Zn 2*p* appears in TPN-COF owing to the usage of the catalyst of $ZnCl_2$, whereas the Co 2*p* signal is obtained for Co-MOF. As for the Co-MOF@TPN-COF composite, the coexistence of Zn 2*p* and Co 2*p* are observed, indicating the combination of TPN-COF and Co-MOF. The Co 2*p*, C 1*s*, and N 1*s* core-level XPS spectra of the Co-MOF@TPN-COF hybrid are also analyzed and illustrated in Fig. 2**e, f,** and **g**, respectively. It displays that two components of Co^{3+} and Co^{2+} are coexisted (Fig. 2**e**), whereas five parts of C-C, C−N, N–C=N, N–C=O, and π–π* binding are observed in the C 1*s* core-level XPS spectrum (Fig. 2**f**). Also, pyridinic, pyrrolic, graphitic N, and NO_x groups are present in the N 1*s* core-level XPS spectrum (Fig. 2**g**). All of these results display that the Co-MOF@TPN-COF hybrid is composed of various functional groups and Co^{2+} and Co^{3+} ions, which are helpful for the aptamer strand immobilization (Mayer, 2009), further boosting the sensing performance. The detailed description of the XPS spectra of Co-MOF, TPN-COF, and Co-MOF@TPN-COF composite were supplied in S3 (See the Supporting information).

3.4. Electrochemical biosensing performances of all samples toward AMP

EIS has been used in many fields of electrochemistry (Kavosi et al., 2015), electrode kinetics (Hu et al., 2004), double-layer studies, batteries (Gordon et al., 2017), corrosion (Ehsani et al., 2017), solid-state electrochemistry and bioelectrochemistry (Jia et al., 2016). As a characterization technique, EIS can provide electric information in the frequency domain. With this technique, a process that occurring in an electrochemical cell can be modeled using a combination of electrical circuits that give the same alternating current response provided by the electrochemical system (Park and Park, 2009). Its wide ability for the characterization of electrode-electrolyte interfaces and its high sensitivity for probing the interfacial properties of a modified electrode surface have made EIS a good alternative for biosensing during the last years. Besides, an important feature presented by the EIS technique is that it does not require any labeled species for the transduction. Thus, it can be used for designing label-free protocols avoiding more expensive and time-consuming assays.

In the present work, the fabrication and detection procedure of the AMP aptasensors based on Co-MOF, TPN-COF, and Co-MOF@TPN-COF were investigated by EIS, as displayed in Fig. 3**a** and S4. The potentials changed with every modified step, which confirms the aptasensor fabrication process. As illustrated in Fig. 3**a**, the bare AE shows a small semicircle diameter (curve *i*, 91 Ω) as expected. After the AE was modified with Co-MOF@TPN-COF composite, the semicircle diameter becomes slightly larger than that of bare AE (curve *ii*, 105 Ω), indicating

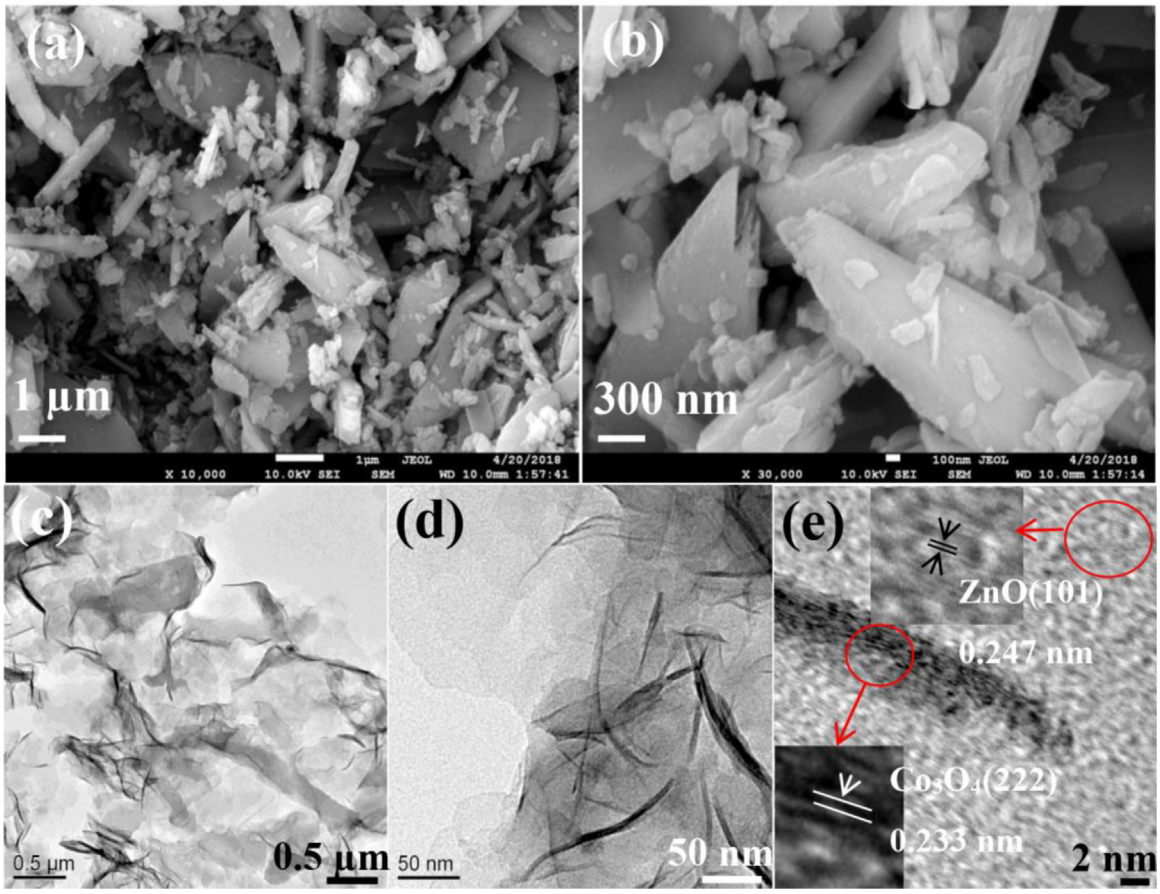

Fig. 1. (a, b) Low- and high-magnification FE-SEM images of Co-MOF@TPN-COF, (c, d, e) TEM and HR-TEM images of Co-MOF@TPN-COF.

that the electron transfer from $[Fe(CN)_6]^{3-/4-}$ to the electrode surface is pretty fast owing to the good conductivity of Co-MOF@TPN-COF. After immobilizing aptamer strands, however, much larger semicircle diameter of Apt/Co-MOF@TPN-COF/AE (curve *iii*, 447 Ω) is observed. It is mainly attributed to the repulsion interaction between the negative charged phosphate groups and the redox couple of $[Fe(CN)_6]^{3-/4-}$, further leading to the slow electron transfer (Top et al., 2016). After incubation of the electrode in AMP target solution, the semicircle diameter increased to 910 Ω (curve *iv*), which is originated from the conformation change of the aptamer strands to bind with AMP molecules, and results in the further decline of the electron transfer (Yang et al., 2017).

As comparison, the Co-MOF- and TPN-COF-based aptasensors were also fabricated to detect AMP (Fig. S6). The same trends are observed, for which the semicircle diameters of the modified AEs increase successively with order of the nanomaterial modification, the aptamer strand immobilization, and the AMP detection. However, the electrode exhibits different semicircle diameters, giving the various R_{ct} values of each step for two detection systems. Furthermore, the detection procedure of AMP using the three kinds of aptasensors based on TPN-COF, Co-MOF, and Co-MOF@TPN-COF also were carried out by CV. As shown in Fig. S7, CV curves of all samples have the typical couple of electrochemical oxidation-reduction peaks. Along with the order of bare AE, the modification of AE with TPN-COF, Co-MOF, and Co-MOF@TPN-COF, respectively, the immobilization of aptamer strands, and the determination of AMP, the peak currents decrease, but giving different peak current changes. The results are consistent with those of EIS for three aptasensors based on TPN-COF, Co-MOF, and Co-MOF@TPN-COF toward AMP.

Additionally, in order to probe the binding kinetics process of AMP with its aptamer in the present sensing system, the impedance spectra of Co-MOF@TPN-COF-based aptasensor incubated with AMP at different periods were carried out, as displayed in Fig. S8a. According to the simulated R_{ct} values, the dependence of R_{ct} on the binding time and rinsing time for the AMP detection using the developed aptasensor was calculated and illustrated in Fig. S8b. For the association rate constant, k_{on}, was calculated from data between 0 and 0.4 h, the R_{ct} value gradually increases with increasing the binding time. Afterward, R_{ct} gradually achieved a plateau, from which the $R_{ct,eq}$ was derived from averaging the values. Moreover, disassociation rate constant k_{off} was calculated from data between 0.67 and 0.93 h. By plotting of $\ln(\Delta R_{ct}/R_{ct,eq})$ as a function of the rinsing time, a straight line was obtained, giving the regression equation of $\ln(\Delta R_{ct}/R_{ct,eq}) = -3.7065\,t - 0.8648$ with a regression coefficient constant of 0.979 (Fig. S8c). As a result, k_{off} can be derived from the slope of the regression equation and evaluated to be 3.7065 h^{-1}. While plotting $\ln(\Delta R_{ct}/R_{ct,eq})$ as a function of the binding time, a straight line was also obtained, giving the regression equation $\ln(\Delta R_{ct}/R_{ct,eq}) = -2.8326\,t - 2.2494$ with the regression coefficient constant of 0.978 (Fig. S8d). Herein, k_{on} can be simulated to 2.1685×10^{-9} M^{-1} h^{-1} regarding to the slope of the regression equation. As a result, the affinity constant, $K_a = k_{on}/k_{off}$ and equals to 5.8505×10^{-10} M^{-1}. As compared with the piezoelectric immunosensor based on polypyrrole (Karaseva and Ermolaeva, 2014), the proposed AMP aptasensor exhibits higher bioaffinity with AMP, thus showing excellent sensing performance.

In order to compare the detection sensitivity of these sensitive nanomaterials, the variation of the R_{ct} values ($\Delta R_{ct} = R_{ct,\,i+1} - R_{ct,\,i}$) of each step for three samples were calculated and illustrated in Fig. 3**b**. Among them, the Co-MOF/AE exhibits the largest ΔR_{ct} value ($R_{ct,\,material} - R_{ct,\,AE}$) of 288 Ω, whereas the Co-MOF@TPN-COF/AE has the smallest ΔR_{ct}, 14 Ω. It indicates that the Co-MOF@TPN-COF composite possesses the superior electrochemical activity to Co-MOF and TPN-

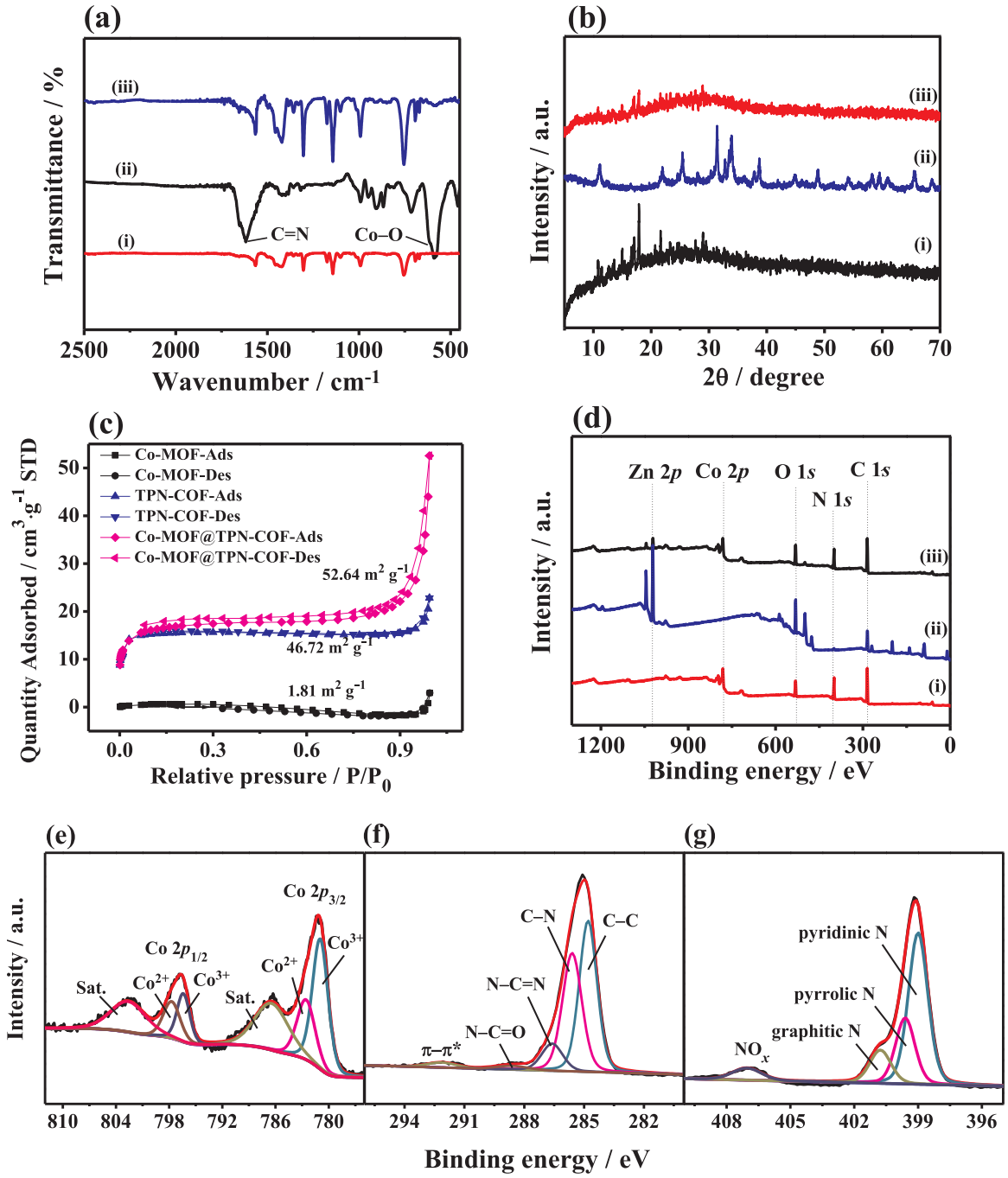

Fig. 2. (a) FT-IR spectra, (b) XRD patterns, (c) XPS survey scan spectra, and (d) Nitrogen adsorption–desorption isotherms of (i) TPN-COF, (ii) Co-MOF, and (iii) Co-MOF@TPN-COF. (c) Co 2*p*, (d) C 1*s*, and (e) N 1*s* core-level XPS spectra of Co-MOF@TPN-COF composite.

COF, which is mainly due to the π-conjugated structure of TPN-COF, and the strong synergistic effect between the rich triazine rings in TPN-COF and framework containing in Co-MOF (Hao et al., 2012). Additionally, the immobilization of aptamer strands over the TPN-COF/AE and Co-MOF/AE lead to the close ΔR_{ct} values, 180 and 210 Ω, respectively. After the detection of AMP, however, the caused ΔR_{ct} values are 175 and 147 Ω for the Apt/TPN-COF/AE and Apt/Co-MOF/AE, respectively. The lower ΔR_{ct} value of the Apt/Co-MOF/AE toward APM hints that the formed G-quadruplex between the AMP and aptamer strands is easily removed from the Co-MOF matrix owning to the weak adsorption interaction between the aptamer strands and Co-MOF. Moreover, it seems that both TPN-COF and Co-MOF do not exhibit good detection sensitivity toward AMP. Therefore, it is necessary to improve this kind of scaffolds materials, further making them behave as superior biosensing aptasensors. Among three kinds of aptasensors, the Co-MOF@TPN-COF/AE causes the highest ΔR_{ct} value ($R_{ct,\ \mathrm{Apt}} - R_{ct,\ \mathrm{material}}$), 342 Ω, illustrating its excellent binding ability and strong interaction with aptamer. As a result, the addition of AMP leads to the maximum R_{ct} variation ($R_{ct,\ \mathrm{AMP}} - R_{ct,\ \mathrm{Apt}}$), 463 Ω. All of these indicate that the Co-MOF@TPN-COF/AE is the most suitable matrix for both aptamer immobilization and detection process. Therefore, the Co-MOF@TPN-COF/AE was chosen for further evaluation of the sensitivity, selectivity, reproducibility, stability, regenerability, and so on.

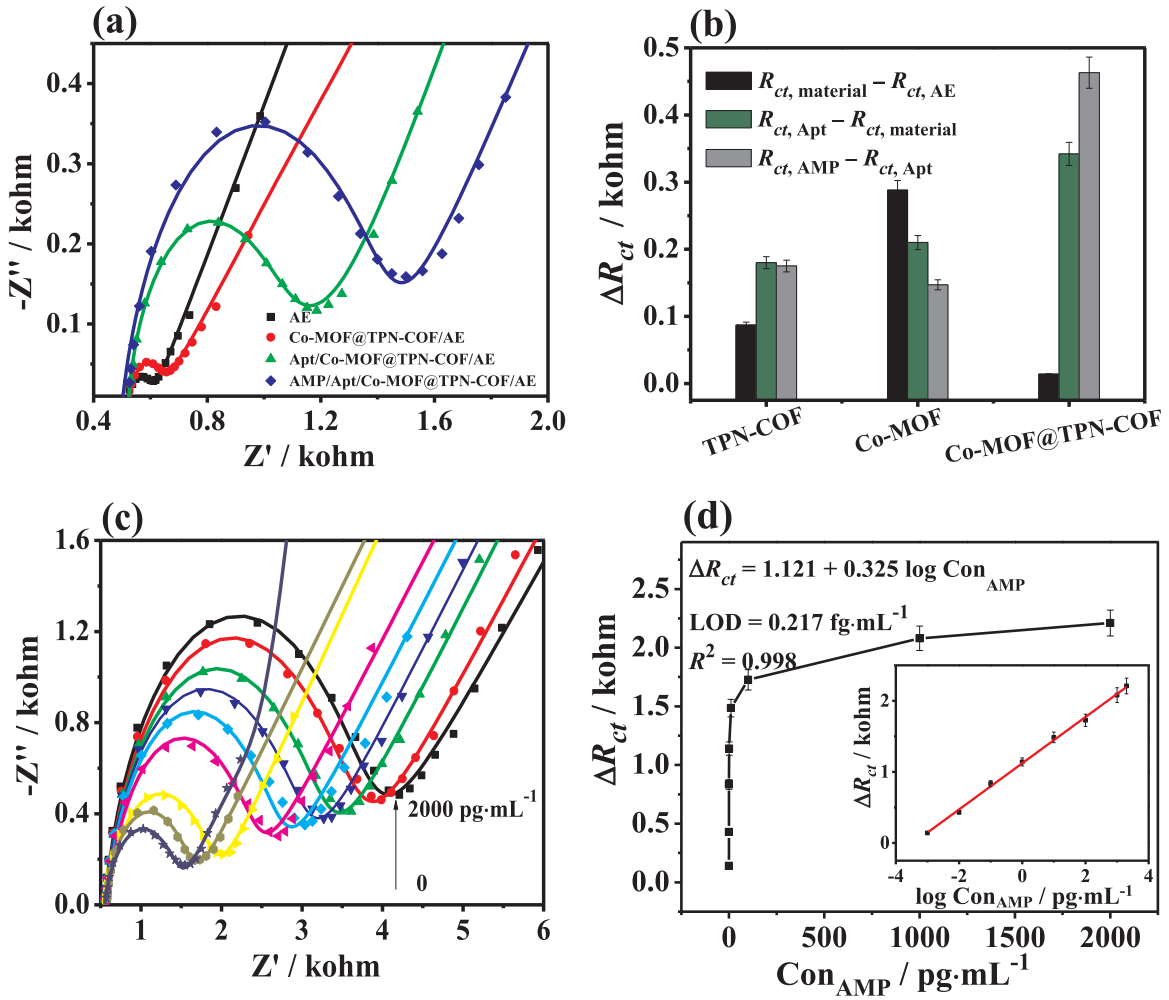

Fig. 3. (a) EIS Nyquist plots of Co-MOF@TPN-COF-modified AEs for detection of AMP including (i) bare AE, (ii) Co-MOF@TPN-COF/AE, (iii) Apt/Co-MOF@TPN-COF/AE, (iv) AMP/Apt/Co-MOF@TPN-COF/AE. (b) Differences in ΔR_{ct} values at each stage for the AMP detection using the TPN-COF-, Co-MOF-, and Co-MOF@TPN-COF-based aptasensors. (c) EIS responses of the Co-MOF@TPN-COF-based aptasenosr with different AMP concentrations (0, 0.001, 0.01, 0.1, 1.0, 10, 100, 1000, and 2000 pg mL^{-1}). (d) Dependence of ΔR_{ct} on the concentration of AMP. The linear parts of the calibration curves are shown in the inset of (d).

3.5. Sensitivity of the Co-MOF@TPN-COF-based aptasensor toward AMP

To investigate the dynamic range of the aptasensor and the detection sensitivity toward AMP, the concentration titration measurements were performed by EIS. Electrolyte solutions were kept under a nitrogen atmosphere during electrochemical measurements through deoxygenating with nitrogen bubbling for at least 30 min. The fabricated aptasensor based on Co-MOF@TPN-COF was first incubated with different concentrations (0.001, 0.01, 0.1, 1, 10, 100, 1000, and 2000 pg mL^{-1}) of AMP for 1 h, and then used for EIS measurements. The EIS spectra were shown in Fig. 3**c**. After adding different concentrations of AMP into the detection system, the R_{ct} values (i.e., the semicircle diameter) of the Co-MOF@TPN-COF-based aptasensor increases with increasing the AMP concentration, which is originated from more and more AMP molecules to bind with the aptamer strands (Yang et al., 2017). As such, it leads to the formation of more G-quadruplex, further resulting in the increase of the electron transfer resistance at the interface between the electrode surface and the electrolyte solution. As expected, the electrochemical EIS responses variation ($R_{ct,\ AMP} - R_{ct,\ Apt}$) was linear with the increasing AMP concentration from 0.001 to 2000 pg mL^{-1}. As illustrated in the inset of Fig. 3**d**, the calibration plot shows a good linear relationship between the ΔR_{ct} responses and the logarithmic value of AMP concentrations. The regression equation is ΔR_{ct} (kohm) = 1.121 + 0.325 log Con_{AMP} (pg mL^{-1}) with a correlation coefficient (R^2) of 0.998. As a result, the calculation equation of the limit of detection (LOD) is listed as: LOD = $3\sigma/s$, where σ is the standard deviation of signal in a blank solution and s is the slope of the calibration curve. In this work, σ was obtained by computing a series of test data (R_{ct}) at the AMP concentration of 0 (i.e., blank solution) at a signal-to-noise (s/n) ratio of 3 (Guo et al., 2010). LOD is estimated to be approximately 0.217 fg mL^{-1} together with the relative standard deviation (RSD) of 2.36%. As compared with other AMP detection approaches (Table 1), the as-fabricated Co-MOF@TPN-COF-based AMP aptasensor exhibits superior detection efficiency with an ultra-low LOD and high sensitivity. The excellent sensing performance of the proposed aptasensor is mainly caused by the following reasons: (i) the synergistic effect between the framework of Co-MOF and the triazine rings of TPN-COF endows the Co-MOF@TPN-COF composite with high electrochemical activity (Zhao et al., 2018); (ii) the strong π–π stacking effect and hydrogen bonding interaction of the high π-conjugated nanostructure of Co-MOF@TPN-COF (Bojdys et al., 2010) and the aptamer strands lead to large amounts of aptamer strands immobilization; and (iii) the mesoporous network of Co-MOF@TPN-COF with high surface specific area can stabilize the formed G-quadruplex between aptamer and AMP, resulting in stable output electrochemical signals.

Table 1
Comparison with other reported techniques for detection of AMP.

Materials	Detection method	Detection Range (pg mL^{-1})	LOD (pg mL^{-1})	Refs.
RU-AMP/thiophenemalonic acid@gold nanoparticles	electrogenerated chemiluminescence	50–10^5	37	(Gui et al., 2015)
Nanoparticulate molecularly imprinted polymers	piezoelectric	10^5–10^6	9×10^4	(Karaseva et al., 2016)
Anti-β-lactam receptors	gold immunochromatographic assay	500–10^4	500	(Chen et al., 2015)
Hairpin probe	differential pulse voltammetry	8.1–1.61 × 10^4	1.61	(Wang et al., 2016a, 2016b)
Gold nanoparticles modified magnetic bead composites	fluorescent spectra	100–10^5	70	(Luo et al., 2017)
Hapten–protein conjugate	piezoelectric	2.5×10^3–5×10^5	3.9×10^3	(Karaseva and Ermolaeva, 2014)
Co-MOF@TPN-COF	EIS	0.001 –2000	0.217 × 10^{-3}	**This work**

3.6. Selectivity, reducibility, stability, and regenerability of the Co-MOF@TPN-COF-based aptasensor

To evaluate the selectivity of the proposed AMP aptasensor based on Co-MOF@TPN-COF composite, eleven other analogues may coexist with AMP in real samples, including ADR, TOB, RFP, Kana, PSA, BSA, Ca^{2+}, Na^+, penicillin, cafazolin, and ring-opened penicillin, were selected as possible interferences. Their concentrations are 1000-folds compared with AMP concentration. According to Fig. 4**a**, it shows that the presence of AMP (0.01 pg mL^{-1}) results in a significant ΔR_{ct} value, while the addition of other interferences (10 pg mL^{-1}) alone causes negligible signal responses, indicating that the developed aptasensor exhibits a satisfactory selectivity. In order to assess whether the fabricated Co-MOF@TPN-COF-based aptasensor can meet the requirements of long-term testing, its reproducibility was measured using five modified electrodes prepared independently under identical condition for EIS measurements. As shown in Fig. 4**b**, the caused ΔR_{ct} responses almost retain the comparable value (RSD = 3.27%, n = 3). Furthermore, the storage stability was evaluated by storing a batch of as-prepared electrodes at 4 °C, which was continuously measured every day for 15 days. As displayed Fig. 4**c**, it was found that about 15% of the initial value was retained after a long storage time of 15 days, suggesting the desirable stability of the developed aptasensor. Also, the regenerability of the fabricated aptasensor was evaluated by immersing the AMP-bound nanocomposite electrode into 0.1 M NaOH at room temperature for 7 min, followed by rinsing with a large amount of Milli-Q water. Afterward, the treated electrode was immersed into the AMP solution (0.001 pg mL^{-1}). Fig. 4**d** shows no substantial change in ΔR_{ct} values of

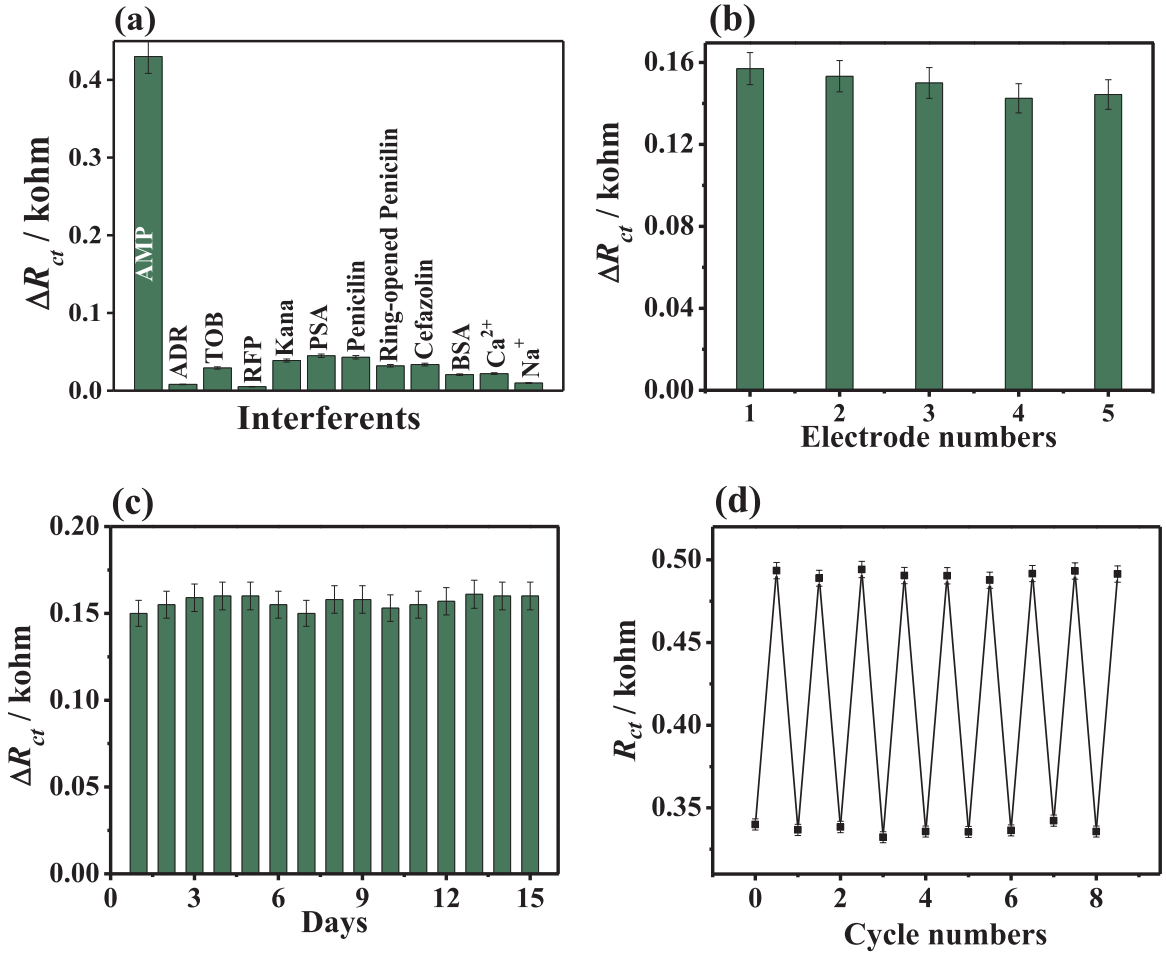

Fig. 4. (a) ΔR_{ct} values of Co-MOF@TPN-COF-based electrochemical aptasensor by separately adding AMP (0.01 pg mL^{-1}) and the interferences (ADR, TOB, RFP, Kana, PSA, BSA, Ca^{2+}, and Na^+ with the concentration of 10 pg mL^{-1}). (b) Reproducibility of the Co-MOF@TPN-COF-based electrochemical aptasensor for detecting AMP (0.001 pg mL^{-1}). (c) Stability and (d) regenerability of the Co-MOF@TPN-COF-based aptasensor for detecting AMP with the concentration of 0.001 pg mL^{-1}.

Table 2
Detection of AMP in human serum, river water and milk samples through the developed aptasensor.

Real samples	Added (pg mL^{-1})	ΔR_{ct} (kΩ)	Found (pg mL^{-1})	Recovery (%)	RSD (%, n = 3)
human serum	0.001	0.14	0.000977	97.7	3.5
	0.01	0.465	0.00961	96.1	4.6
	0.1	0.79	0.09587	95.9	3.9
	1	1.115	0.9561	95.6	2.1
	10	1.44	9.55	95.5	4.1
	100	1.772	99.885	99.9	3.5
	1000	2.092	961.61	96.2	5.1
river water	0.001	0.15	0.001034	103.4	2.5
	0.01	0.475	0.01032	103.2	2.9
	0.1	0.8	0.1028	102.8	4.3
	1	1.125	1.02609	102.6	3.8
	10	1.45	10.234	102.3	4.3
	100	1.775	102.0444	102.0	3.5
	1000	2.095	982.245	98.2	2.8
milk	0.001	0.148	0.001020	102.0	4.3
	0.01	0.474	0.010244	102.5	3.4
	0.1	0.796	0.10002	100.0	2.6
	1	1.125	1.02609	102.6	2.8
	10	1.445	9.87692	98.8	4.2
	100	1.767	96.42809	96.4	5.1
	1000	2.098	1003.33	100.3	3.8

the proposed aptasensor during the eight regeneration runs. This observation indicates that the aptasensor could be facilely regenerated. All results reveal that the fabricated aptasensor exhibits high sensitivity, excellent selectivity, acceptable reproducibility, high stability, and excellent regenerability.

3.7. Analysis of human serum, river water and milk samples

In order to evaluate its applicability in real sample analysis, our method was employed to determine AMP residues in 500-fold-diluted human serum, river water, and milk. As could be seen in Table 2, the recovery for human serum sample varies from 95.5% to 99.9% and the RSD varies from 2.1% to 5.1%; the recovery for river water sample varies from 98.2% to 103.4% and the RSD varies from 2.5% to 4.3%, while the recovery for milk sample changes from 96.4% to 102.6% and the RSD varies from 2.6% to 5.1%. The results indicate that the proposed aptasensor for AMP detection has the potential applied value in real samples. Thus, this method shows great potential for practical use in determination of AMP residues in real samples.

4. Conclusion

In summary, we have constructed a novel ultrasensitive aptasensing platform based on the composite of Co-MOF and TPN-COF for determining the antibiotic residue in human serum, river water and milk. The proposed Co-MOF@TPN-COF not only exhibits high specific surface area (52.64 m^2 g^{-1}) but also possesses nitrogen-rich groups and triazine rings, thus resulting in large amounts of aptamer strand adsorption owning to the strong binding forces between aptamer strands and the Co-MOF@TPN-COF matrix. Compared with the individual Co-MOF and TPN-COF, the Co-MOF@TPN-COF-based aptasensor shows an extreme low detection limit (0.217 fg mL^{-1}) toward AMP within the concentration from 0.001 to 2000 pg mL^{-1} because of its excellent electrochemical performance and signal amplification. Concurrently, the proposed aptasensor also features excellent selectivity owing to the high specificity of the aptamer, along with good reproducibility, high stability, acceptable regenerability, and favorable applicability in human serum, river water and milk. Therefore, the proposed Co-MOF@TPN-COF-based aptasensor has great potential for application in food safety field.

Acknowledgment

This work was supported by Programs for the National Natural Science Foundation of China, China (NSFC: Account Nos. U1604127 and U1704256), and Innovative Technology Team of Henan Province, China (CXTD2014042).

Appendix A. Supporting information

Supplementary data associated with this article can be found in the online version at doi:10.1016/j.bios.2018.09.089.

References

Bojdys, M.J., Jeromenok, J., Thomas, A., Antonietti, M., 2010. Adv. Mater. 22, 2202–2205.
Bunka, D.H.J., Stockley, P.G., 2006. Nat. Rev. Microbiol. 4, 588–596.
Chakraborty, K., Thilakan, B., Kizhakkekalam, V.K., 2018. J. Appl. Microbiol. 124, 108–125.
Chan-Thaw, C.E., Villa, A., Katekomol, P., Su, D., Thomas, A., Prati, L., 2010. Nano Lett. 10, 537–541.
Chen, H., Qiu, Q., Sharif, S., Ying, S., Wang, Y., Ying, Y., 2018. ACS Appl. Mater. Interfaces 10, 24108–24115.
Chen, Y., Zhang, R., Jiao, L., Jiang, H., 2018. Coord. Chem. Rev. 362, 1–23.
Chen, Y., Wang, Y., Liu, L., Wu, X., Xu, L., Kuang, H., Li, A., Xu, C., 2015. Nanoscale 7, 16381–16388.
Clarke, S.J., Littleford, R.E., Smith, W.E., Goodacre, R., 2005. Analyst 130, 1019–1026.
Das, S., Sarkar, H.S., Uddin, M.R., Rissanen, K., Mandal, S., Sahoo, P., 2017. Chem. Commun. 53, 7600–7603.
Drawz, S.M., Bonomo, R.A., 2010. Clin. Microbiol. Rev. 23, 160–201.
Ehsani, A., Mahjani, M.G., Hosseini, M., Safari, R., Moshrefi, R., Mohammad Shiri, H., 2017. J. Colloid Interface Sci. 490, 444–451.
Feng, L., Liu, M., Liu, H., Fan, C., Cai, Y., Chen, L., Zhao, M., Chu, S., Wang, H., 2018. ACS Appl. Mater. Interfaces 10, 23647–23656.
Feng, X., Ding, X., Jiang, D., 2012. Chem. Soc. Rev. 41, 6010–6022.
Fu, J., Das, S., Xing, G., Ben, T., Valtchev, V., Qiu, S., 2016. J. Am. Chem. Soc. 138, 7673–7680.
Gordon, I.A.J., Grugeon, S., Takenouti, H., Tribollet, B., Armand, M., Davoisne, C., Débart, A., Laruelle, S., 2017. Electrochim. Acta 223, 63–73.
Gross, A.F., Sherman, E., Vajo, J.J., 2012. Dalton Trans. 41, 5458–5460.
Gui, G., Zhuo, Y., Chai, Y., Xiang, Y., Yuan, R., 2015. Biosens. Bioelectron. 70, 221–225.
Guo, C., Su, F., Song, Y., Hu, B., Wang, M., He, L., Peng, D., Zhang, Z., 2017. ACS Appl. Mater. Interfaces 9, 41188–41199.
Guo, L., Zhong, J., Wu, J., Fu, F., Chen, G., Zheng, X., Lin, S., 2010. Talanta 82, 1654–1658.
Hao, L., Luo, B., Li, X., Jin, M., Fang, Y., Tang, Z., Jia, Y., Liang, M., Thomas, A., Yang, J., Zhi, L., 2012. Energy Environ. Sci. 5, 9747–9751.
Hu, J., Zhang, J., Cao, C., 2004. Int. J. Hydrog. Energy 29, 791–797.
Jia, X., Dong, S., Wang, E., 2016. Biosens. Bioelectron. 76, 80–90.
Jiang, D., Hu, T., Zheng, H., Xu, G., Jia, Q., 2018. Chem. -Eur. J. 0.
Karaseva, N., Ermolaeva, T., Mizaikoff, B., 2016. Sens. Actuators B-Chem. 225, 199–208.
Karaseva, N.A., Ermolaeva, T.N., 2014. Talanta 120, 312–317.
Kavosi, B., Salimi, A., Hallaj, R., Moradi, F., 2015. Biosens. Bioelectron. 74, 915–923.
Klug, S.J., Famulok, M., 1994. Mol. Biol. Rep. 20, 97–107.
Kreno, L.E., Leong, K., Farha, O.K., Allendorf, M., Van Duyne, R.P., Hupp, J.T., 2012. Chem. Rev. 112, 1105–1125.
Kuhn, P., Antonietti, M., Thomas, A., 2008a. Angew. Chem. Int. Ed. 47, 3450–3453.
Kuhn, P., Forget, A., Su, D., Thomas, A., Antonietti, M., 2008b. J. Am. Chem. Soc. 130, 13333–13337.
Lan, L., Yao, Y., Ping, J., Ying, Y., 2017. ACS Appl. Mater. Interfaces 9, 23287–23301.
Lee, J., Farha, O.K., Roberts, J., Scheidt, K.A., Nguyen, S.T., Hupp, J.T., 2009. Chem. Soc. Rev. 38, 1450–1459.
Li, W., Yang, C., Yan, X., 2017. Chem. Commun. 53, 11469–11471.
Lin, C., Zhang, D., Zhao, Z., Xia, Z., 2017. Adv. Mater. 30, 1703646.
Luo, Z., Wang, Y., Lu, X., Chen, J., Wei, F., Huang, Z., Zhou, C., Duan, Y., 2017. Anal. Chim. Acta 984, 177–184.
Mayer, G., 2009. Angew. Chem. Int. Ed. 48, 2672–2689.
Meng, H., Liu, H., Kuai, H., Peng, R., Mo, L., Zhang, X., 2016. Chem. Soc. Rev. 45, 2583–2602.
Moura, F., de Almeida, F.G., Rebelo, L.B., Bezerra, C.Q., 2012. J. Sep. Sci. 35, 2615–2620.
Ning, W., Di, Z., Yu, Y., Zeng, P., Di, C., Chen, D., Kong, X., Nie, G., Zhao, Y., Li, L., 2018. Small 14, 1703812.
Palchetti, I., Mascini, M., 2012. Anal. Bioanal. Chem. 402, 3103–3114.
Park, J., Park, S., 2009. Sensors-Basel 9, 9513–9532.
Peng, Y., Huang, Y., Zhu, Y., Chen, B., Wang, L., Lai, Z., Zhang, Z., Zhao, M., Tan, C., Yang, N., Shao, F., Han, Y., Zhang, H., 2017a. J. Am. Chem. Soc. 139, 8698–8704.
Peng, Y., Zhao, M., Chen, B., Zhang, Z., Huang, Y., Dai, F., Lai, Z., Cui, X., Tan, C., Zhang, H., 2017b. Adv. Mater. 30, 1705454.
Qi, Y., Zhang, H., Du, N., Yang, D., 2013. J. Mater. Chem. A 1, 2337–2342.
de Silva, A.P., Gunaratne, H.Q.N., Gunnlaugsson, T., Huxley, A.J.M., McCoy, C.P., Rademacher, J.T., Rice, T.E., 1997. Chem. Rev. 97, 1515–1566.

Shi, Q., Chen, Z., Song, Z., Li, J., Dong, J., 2010. Angew. Chem. 123, 698–701.
Su, F., Zhang, S., Ji, H., Zhao, H., Tian, J., Liu, C., Zhang, Z., Fang, S., Zhu, X., Du, M., 2017. ACS Sens. 2, 998–1005.
Tan, B., Zhao, H., Wu, W., Liu, X., Zhang, Y., Quan, X., 2017. Nanoscale 9, 18699–18710.
Tombelli, S., Minunni, M., Mascini, M., 2005. Biosens. Bioelectron. 20, 2424–2434.
Top, M., Er, O., Congur, G., Erdem, A., Lambrecht, F.Y., 2016. Talanta 160, 157–163.
Vasilescu, A., Marty, J., 2016. TrAC-Trend Anal. Chem. 79, 60–70.
Wang, H., Wang, Y., Liu, S., Yu, J., Xu, W., Guo, Y., Huang, J., 2015. Chem. Commun. 51, 8377–8380.
Wang, J., Ma, K., Yin, H.S., Zhou, Y.L., Ai, S.Y., 2018. Microchim. Acta 185, 68.
Wang, X., Dong, S., Gai, P., Duan, R., Li, F., 2016. Biosens. Bioelectron. 82, 49–54.
Wang, Z., Yu, J., Gui, R., Jin, H., Xia, Y., 2016. Biosens. Bioelectron. 79, 136–149.
Wen, Y., Meng, W., Li, C., Dai, L., He, Z., Wang, L., Li, M., Zhu, J., 2018. Dalton Trans. 47, 3872–3879.
Xia, W., Li, J., Wang, T., Song, L., Guo, H., Gong, H., Jiang, C., Gao, B., He, J., 2018. Chem. Commun. 54, 1623–1626.
Xie, S., Ye, J., Yuan, Y., Chai, Y., Yuan, R., 2015. Nanoscale 7, 18232–18238.
Xiong, S., Chen, J.S., Lou, X.W., Zeng, H.C., 2011. Adv. Funct. Mater. 22, 861–871.
Yang, Q., Lu, R., Ren, S., Chen, C., Chen, Z., Yang, X., 2018. Chem. Eng. J. 348, 202–211.
Yang, Z., Ding, X., Guo, Q., Wang, Y., Lu, Z., Ou, H., Luo, Z., Lou, X., 2017. Sens. Actuators B-Chem. 253, 1129–1136.
Yu, Z., Lai, R.Y., 2018. Talanta 176, 619–624.
Yu, Z., Sutlief, A.L., Lai, R.Y., 2018. Sens. Actuators B-Chem. 258, 722–729.
Zhang, Z., Duan, F., Tian, J., He, J., Yang, L., Zhao, H., Zhang, S., Liu, C., He, L., Chen, M., Chen, D., Du, M., 2017a. ACS Sens. 2, 982–989.
Zhang, Z., Ji, H., Song, Y., Zhang, S., Wang, M., Jia, C., Tian, J., He, L., Zhang, X., Liu, C., 2017b. Biosens. Bioelectron. 94, 358–364.
Zhang, Z., Dong, L., Zhu, Q., 2018. Electrochim. Acta 282, 588–594.
Zhao, F., Liu, H., Mathe, S., Dong, A., Zhang, J., 2018. Nanomaterials 8, 15.
Zhao, M., Wang, Y., Ma, Q., Huang, Y., Zhang, X., Ping, J., Zhang, Z., Lu, Q., Yu, Y., Xu, H., Zhao, Y., Zhang, H., 2015. Adv. Mater. 27, 7372–7378.
Zhu, C., Yang, G., Li, H., Du, D., Lin, Y., 2015. Anal. Chem. 87, 230–249.
Zhuang, G., Gao, Y., Zhou, X., Tao, X., Luo, J., Gao, Y., Yan, Y., Gao, P., Zhong, X., Wang, J., 2017. Chem. Eng. J. 330, 1255–1264.